

## Microfracturing, damage, and failure of brittle granites

Oded Katz<sup>1</sup> and Ze'ev Reches

Institute of Earth Sciences, Hebrew University, Jerusalem, Israel

Received 7 May 2002; revised 25 September 2003; accepted 17 October 2003; published 20 January 2004.

[1] The evolution of stress-induced damage and the eventual brittle failure are experimentally analyzed for Mount Scott granite of Oklahoma. We quantify the damage intensity in two methods and directly compare model predictions and actual damage. The 14 samples of the medium-grain-size granite were loaded triaxially at dry conditions, room temperature, and under 41 MPa confining pressure.

Microfractures were mapped in five samples, and the majority of them (80%) belong to two groups: tensile microfractures trending subparallel to the loading axis and shear microfractures trending 11°–40° off the loading axis. The tensile microfractures dominate the low-stress stage, and they remain intragranular with a stress increase. The relative density of shear microfractures increases with increasing stresses, and they formed elongated, intergranular zones of coalescing microfractures. We compared two independent values of damage intensity: (1) the macroscopic, experimentally measured reduction of the deformation modulus and (2) the expected reduction of this modulus calculated with several damage models for the density of the mapped microfractures. Our fracture density data best fit the model of noninteracting cracks of *Kachanov* [1992]. **INDEX TERMS:** 8010 Structural Geology: Fractures and faults; 8020 Structural Geology: Mechanics; 8030 Structural Geology: Microstructures; **KEYWORDS:** brittle, failure, damage, microfracture, shear, nonlinear

**Citation:** Katz, O., and Z. Reches (2004), Microfracturing, damage, and failure of brittle granites, *J. Geophys. Res.*, 109, B01206, doi:10.1029/2002JB001961.

### 1. Introduction

[2] Loading of brittle rocks leads to the development of distributed damage long before the rock fails unstably. This damage was used to explain a range of phenomena: reduction of seismic wave velocity [*Nur and Simmons*, 1969], seismic anisotropy [*Scott et al.*, 1994; *Crampin*, 1994], reduction of elastic moduli [*Budiansky and O'Connell*, 1976; *Kachanov*, 1992; *Lyakhovskiy et al.*, 1997a, 1997b], and rock failure [*Ashby and Sammis*, 1990; *Reches and Lockner*, 1994]. Theoretical analyses of damage characteristics are based on fundamental principles [*Lyakhovskiy et al.*, 1997a, 1997b; *Turcotte et al.*, 2003] and on physical features like microfractures [*Sayers and Kachanov*, 1995; *Kachanov*, 1992; *Crampin*, 1994]. Damage intensity can be evaluated by indirect, acoustic emission analysis [*Cox and Meridith*, 1993], or by direct, microstructural observations of deformed rocks; for example the analyses of microfractures and dilational microcracks [*Hadley*, 1976; *Tapponnier and Brace*, 1976; *Kranz*, 1979; *Reches and Lockner*, 1994]. Typically, these microfractures are smaller than the grain size [*Hadley*, 1976], and they are often quasi-uniformly distributed prior to faulting [*Lockner et al.*, 1992]. Local, nonuniform distri-

butions of microfractures are apparently related to fault nucleation and growth [*Reches and Lockner*, 1994]. To the best of our knowledge, there was no attempt to compare theoretical damage parameters (e.g., microfracture density of *Kachanov* [1992]) that are determined from experimental stress-strain relations, and the corresponding, actual density of microfractures that can be measured independently in the stressed rocks. It is apparent that such comparison is essential for testing theoretical models and usage of their predictions [*Crampin and Sayers*, 1994]. This quantitative comparison between parameters derived from damage models and direct observations of microscopic damage is the central objective of the present study.

[3] We conducted a series of triaxial experiments with brittle granite samples and determined two independent indicators of the stress-induced damage. The first includes rheological parameters (deformation modulus and volumetric strain) that were monitored during the triaxial loading; these parameters are the macroscopic expressions of the internal, distributed damage. The second indicator includes the distribution, orientations and intensity of the microfractures mapped in the deformed samples; these parameters are the physical manifestation of the same damage. We start by outlining the experimental procedures followed by descriptions of the macroscopic rheology and microstructural mapping. These observations are then analyzed in terms of damage and failure models.

<sup>1</sup>Also at Geological Survey of Israel, Jerusalem, Israel.

**Table 1.** Experimental Stress-Strain Relations<sup>a</sup>

Test	Specimen Length, mm	Hold Time, <sup>b</sup> min	Hold Stress, <sup>c</sup> MPa	Failure Stress, MPa	Maximum NDS <sup>d</sup>	$E$ , <sup>e</sup> GPa	$\nu$ <sup>e</sup>	Comments
101	66.9			613	1.05	70	0.18	load to failure
102	63.5	95	601		1.03	74	0.21	load hold
103	93.8			595	1.02	72	0.22	load to failure
104	93.7	61	613	528	1.05	77	0.17	spontaneous failure
105	99.0	180	467		0.80	72	0.22	cycle 1
				636	1.09	74	0.29	load to failure
106	96.1	1.25	592	517	1.01	73	0.22	spontaneous failure
108	100.2	180	505		0.86	80	0.20	load hold
109	98.1	180	546		0.93	72	0.18	load hold
110	94.5	0.03	564	561	0.96	73	0.19	spontaneous failure
112	90.9			573	0.98	72	0.21	load to failure
113	96.1	180	563		0.96	70	0.20	load hold
114	96.6	180	518		0.88	72	0.21	load hold
115	93.4	360	534		0.91	74	0.21	load hold
116	97.1	180	460		0.78	74	0.22	load hold
117	89.4	180	318		0.54	71	0.21	load hold
123	95.4	180	334		0.57	71	0.22	load hold
124	76.0				0.95	71	0.18	cycle 1
					0.96	68	0.22	cycle 2
				657	1.12	67	0.26	load to failure
125	83.2	180	546		0.93	70	0.20	cycle 1
				617	1.05	68	0.27	load to failure

<sup>a</sup>The results of seven tests (107, 111, and 118–122) are not included in the analysis due to technical problems during the experiments.

<sup>b</sup>Time elapsed from start of stroke holding to unload or to failure.

<sup>c</sup>Maximum stress at the start of holding.

<sup>d</sup>Normalized differential stress at hold point or at failure (equation (2) in text).

<sup>e</sup>Calculated before the onset of dilation.

Finally, we discuss the effects of damage evolution on the failure mechanism.

## 2. Experimental Procedure

### 2.1. Mount Scott Granite

[4] We used samples of Mount Scott granite, MSG, of Wichita Mountains, southwestern Oklahoma. The MSG has a porphyritic texture with ovoid anorthoclase phenocrysts in a matrix of alkali feldspar and quartz, and it includes small amounts of hornblende, biotite and iron oxides [Price *et al.*, 1996]. It is a fine-grained to medium-grained rock with mean grain size of  $0.9 \pm 0.2$  mm and dry density of  $2645 \text{ kg/m}^3$ . The tested samples are from an unaltered and only slightly fractured core drilled at depth of about 50 m (details by Price *et al.* [1998]).

[5] The mechanical properties of MSG of this core were determined by Katz *et al.* [2001] in a series of 13 uniaxial and triaxial loading-to-failure tests under confining pressure up to 66 MPa. The Young's modulus increases, linearly, from 75 GPa for the uniaxial tests, to 82 GPa at 66 MPa confining pressures, and the Poisson's ratio is 0.26–0.31 at low confining pressure and it decreases to about 0.21 with increasing confining pressure. The determined Coulomb strength of MSG is [Katz *et al.*, 2001]

$$\sigma_1 = 270 + 8.7\sigma_3 \text{ (in MPa)} \quad (1a)$$

$$\tau = 46 + 1.31\sigma_N \text{ (in MPa)}. \quad (1b)$$

[6] The patterns of failure surfaces vary with the increasing confining pressure. Axial splitting with few major fractures and numerous minor cracks dominated the uniaxial tests. Under the lower confining pressures of 14–28 MPa, the fractures display a diffuse pattern of a few major faults and numerous smaller cracks, whereas under confining pressures

of 41–66 MPa fewer cracks appear along with the major fault. The angle between the normal to the major faults and the direction of the maximal compressive stress ( $\sigma_1$ ), measured on the faulted core samples, is  $68^\circ$ – $75^\circ$ .

### 2.2. Experimental Setup

[7] The tests were performed on 25.4 mm diameter cylinders drilled into the field core (45.5 mm in diameter) and parallel to its long axis. The tested samples have a length-to-diameter ratio of 2.5–3.9, and perpendicularity  $\leq 0.005$  radians. A “dog bone” epoxy structure was added to the specimen ends to fit it to the 38.1 mm diameter of the loading end pieces. Samples were oven-dried ( $110^\circ\text{C}$ ) for at least 24 hours. Heat shrink tubing was used to jacket the specimen. We used a 69 MPa pressure vessel (SBEL model RC10) and the axial load was supplied by a stiff ( $9 \times 10^9 \text{ N/m}$ ), servo-controlled hydraulic load frame (MTS model 315) with a 2669 kN actuator. Stroke and confining pressure intensifiers were controlled using a MTS microprofilers model 458.91. Load was monitored using an internal load cell at the lower part of the load frame. Axial displacement of the core was monitored by using two LVDTs attached to the end pieces, and the lateral displacement was monitored by using a chain extensometer (MTS model 632.92B-05) at the middle of the core height.

[8] All tests were performed under confining pressure of 41 MPa (Table 1), for which the Coulomb strength is  $U_S = 586 \pm 16$  MPa (equation (1)). The experimentally measured differential stress,  $(\sigma_1 - \sigma_3)$ , is replaced by its normalized value, NDS (Normalized Differential Stress):

$$\text{NDS} = (\sigma_1 - \sigma_3)/U_S = (\sigma_1 - \sigma_3)/586. \quad (2)$$

The NDS values at failure in the present experiments range between 0.96 and 1.05, reflecting the inherent inhomogeneity of the samples and the deviations from  $U_S$ .

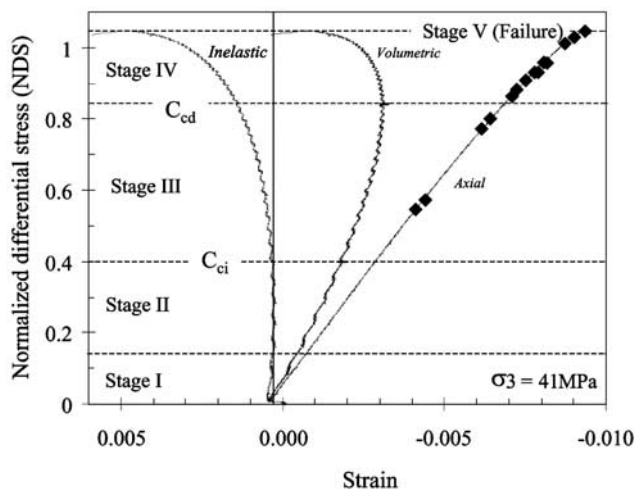


**Figure 1.** Stress-strain relations of test 101 that are typical for the present experiments (compressive strain is negative). The stress axis is marked by NDS (normalized differential stress, equation (2)); the curves are for axial strain, total volumetric strain and crack (inelastic) volumetric strain (CVS, equation (4)). The curves display several stages marked following *Wawersik and Brace* [1971]: I, nonlinear stress increase associated with cracks closure; II, quasi-linear elastic stage; III, nonlinear stress increase associated with crack growth and dilation; IV, failure stage with increase of crack growth; and V, failure.  $C_{ci}$  is the crack initiation stress where dilation begins;  $C_{cd}$  is the crack damage stress where failure initiates. Solid diamonds present the maximal NDS of each test in the series.

[9] We performed 14 load-hold tests and each test consists of five steps: (1) confining pressure loading at a constant rate of 0.023 MPa/s; (2) axial loading to a preselected stress that ranges from NDS = 0.54 to NDS = 1.05 (Table 1). Axial shortening was at a strain rate of  $\sim 1 \times 10^{-5} \text{ s}^{-1}$ . (3) Once the preselected stress was achieved, the specimen was held at a constant stroke for up to 6 hours. Eleven of the samples did not fail during the hold time and three failed spontaneously (Table 1). (4) After the hold period, the samples were unloaded by first reducing the axial stress to the confining pressure and then decreasing both stresses at the loading rates; (5) three of the unfailed samples were cyclically loaded up to failure after the hold period.

### 3. Macroscopic Experimental Results

#### 3.1. Strain-Stress Relations and the Deformation Modulus

[10] Figure 1 shows the typical stress-strain curves of the present experiments. It displays several stages that were recognized previously [*Wawersik and Brace*, 1971]. Stage I, at the range of  $0 < \text{NDS} < 0.15$ , includes the nonlinear stress increase associated with cracks closure. Stage II, at  $0.15 < \text{NDS} < 0.40$ , displays apparently linear elastic curve. Stages III and IV start at  $\text{NDS} \approx 0.4$  ( $C_{ci}$ , crack initiation stress [*Martin and Chandler*, 1994]) and  $\text{NDS} \approx 0.85$  ( $C_{cd}$ , crack damage stress [*Martin and Chandler*, 1994]), respectively, are characterized by first

stable (stage III) and then unstable (stage IV) stress increase associated with crack growth and dilation. Stage V is the failure stage of  $\text{NDS} \approx 1.0$  with initial stable stress decrease followed by unstable stress drop.

[11] The stress-strain curve is analyzed in terms of the deformation modulus,  $D$ :

$$D = d(\sigma_1 - \sigma_3)/d\varepsilon, \quad (3a)$$

where  $\varepsilon$  is the axial strain. The parameter  $D$  is the local slope of the stress-strain curve and it is equivalent to Young's modulus,  $E$ , of the recoverable, elastic strain. Unlike  $E$ , the deformation modulus may also include permanent, inelastic deformation that is attributed to pervasive stress-induced damage. To remove temporal noise, the  $D$  values are calculated as the derivative of least squares regression fit by a six-order polynomial to the experimental stress-strain curve. The cyclical reloading (Table 1) indicated that  $E$  does not change significantly during reloading to  $\text{NDS} < 0.95$  and the Poisson's ratio  $\nu$  increases with cyclic reloading (based on four observations).

[12] Figure 2 presents  $D$  curves of five tests with holding stresses of  $\text{NDS} = 0.54$ – $1.01$  (the last failed spontaneously) and of one test that loaded to failure. The  $D$  curves of the other tests are similar and they were omitted for clarity. At stresses below  $\text{NDS} \sim 0.1$ , the  $D$  variations are inconsistent; even though  $D$  is expected to increase due to cracks closure, it decreases in a few tests (101, 106, 125) (Figure 2). All tests display a distinct maximum of

$$D_{\max} = 74 \pm 3 \text{ GPa} \quad (3b)$$

at  $\text{NDS} = 0.19 \pm 0.06$  (Table 2). The  $D$  values decrease for stresses of  $\text{NDS} > 0.19$ . The decrease rate is modest up to the transition stage of  $\text{NDS} = 0.81 \pm 0.03$  when  $D$  decreases at an accelerated constant rate until failure at

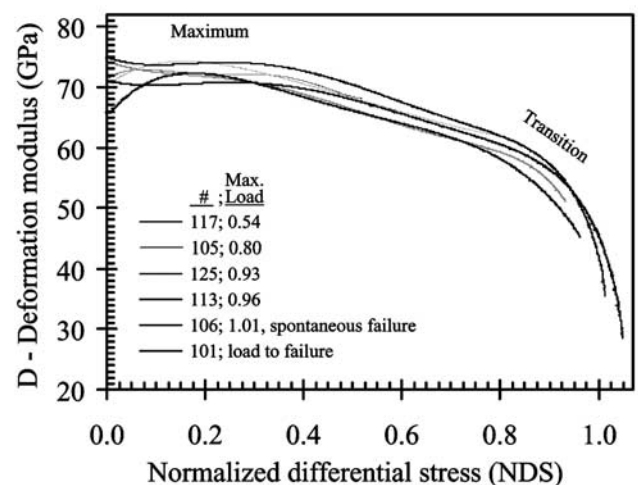


**Figure 2.** Deformation modulus,  $D$ , (equation (3a)) as a function of normalized stress (NDS) for six tests (117, 105, 125, 113, 106, 101) covering the loading range of  $\text{NDS} = 0.54$ – $1.01$ . The results of the other eight tests are similar and are not shown for clarity. Maximum, the stage in which  $D$  attains its maximum value,  $D_{\max}$ ; Transition, stage in which  $D$  reduction is accelerated.

**Table 2.** Experimental Deformation Modulus Results

Test	Plateau Values (Maximum Deformation Modulus) <sup>a</sup>		Transition Stage of the Deformation Modulus <sup>b</sup>		Maximum Stress (NDS) <sup>c</sup>	Deformation Modulus at Failure, GPa
	NDS	GPa	NDS	GPa		
101	0.17	71	0.83	60	1.05	29
102			0.83	60	1.03	45
103			0.82	56	1.02	19
104			0.79	65	1.05	41
105	0.15	74			0.80	
			0.59	73	1.09	32
106	0.24	74	0.83	69	1.01	36
108	0.24	81	0.80	64	0.86	
109	0.15	73	0.83	60	0.93	
110	0.05	76	0.77	61	0.96	49
112	0.25	74	0.81	61	0.98	48
113	0.17	72	0.75	61	0.96	
114	0.27	74	0.84	59	0.88	
115	0.22	78	0.79	60	0.91	
116	0.15	80			0.78	
117	0.17	72			0.54	
123	0.21	74	0.50	68	0.57	
124	0.15	73			0.95	
			0.76	65.1	0.96	
			0.80	65	1.14	11
125	0.12	72	0.84	58	0.93	
	0.27	69	0.82	66	1.05	37

<sup>a</sup>Plateau values are for the stage when the Deformation modulus reaches its maximum value (Figure 2, see text).

<sup>b</sup>Transition stage refers to the stress in which the reduction rate of the Deformation modulus increases (see the transition from gentle slope to steep slope in Figure 2).

<sup>c</sup>Stress values are presented as NDS (equation (2), see text).

NDS =  $1.0 \pm 0.05$  (Figure 2). The deformation modulus at the transition is  $63 \pm 4$  GPa. The modulus just before failure in samples loaded to failure is not well constrained; it is less than 50 GPa and in some samples even less than 30 GPa.

[13] The samples were subjected to load-hold loading with holding periods up to 6 hours. All 11 samples with maximum loading of NDS < 0.96 did not fail during the hold periods while the three samples loaded with NDS  $\geq 0.96$  failed spontaneously (with the exception of test 102). It appears that NDS  $\approx 0.96$  is an apparent threshold for spontaneous failure.

### 3.2. Crack Volumetric Strain (CVS)

[14] The macroscopic effect of growth and dilation of microcracks can be evaluated by the crack volumetric strain, CVS. The CVS is the inelastic strain manifested as the difference between the total experimental volumetric strain,  $(\varepsilon_V)_{\text{experimental}}$ , measured during axial loading and the elastic volumetric strain,  $(\varepsilon_V)_E$  for this stage [e.g., *Martin and Chandler, 1994*]:

$$\text{CVS} = (\varepsilon_V)_{\text{experimental}} - (\varepsilon_V)_E. \quad (4)$$

[15] The elastic volumetric strain during loading is

$$(\varepsilon_V)_E = (\sigma_1 - \sigma_3)(1 - 2\nu)/E \quad (5a)$$

because from Hooke's expression for the elastic volumetric strain,

$$(\varepsilon_V)_E = (\sigma_1 + \sigma_2 + \sigma_3)(1 - 2\nu)/E, \quad (5b)$$

one has to subtract the elastic volumetric strain due to initial compaction by the confining pressure,

$$(\varepsilon_V)_{E,\text{confining}} = 3\sigma_3(1 - 2\nu)/E. \quad (5c)$$

[16] Following others [*Nur and Simmons, 1969; Martin and Chandler, 1994*], we interpret the CVS as reflecting microcrack opening. A curve of CVS is shown in Figure 1 and it also displays the four steps of Figure 1: Stage I, CVS decreases due to crack closure; stage II the apparent elastic loading, no change in CVS; stages III and IV, CVS increases nonlinearly due to growth and dilation of microcracks.

[17] Figure 3 presents two forms of CVS values. In the first, a single CVS value is determined for each sample by using its  $E$  and  $\nu$ . The values are calculated for the stress at holding period in the stable tests (solid symbols in Figure 3) or for the stress just before failure for the failed tests (open symbols). The second form presents the continuous variations of CVS during a single test (test 106) (curve in Figure 3). Several important features can be noted in Figure 3. First, the CVS values of the individual tests agree well with the continuous curve of test 106 for the range of NDS  $\leq 0.95$ , and it increases monotonously for NDS  $\leq 0.95$  according to the empirical relations

$$\text{CVS} = 4 \times 10^{-6} e^{6.2\text{NDS}}, \quad (6)$$

reaching a value of CVS  $\approx 0.0015$  at NDS = 0.95. Second, for NDS > 0.95, the CVS is poorly constrained within the range of  $0.001 < \text{CVS} < 0.005$ . We interpret this observation

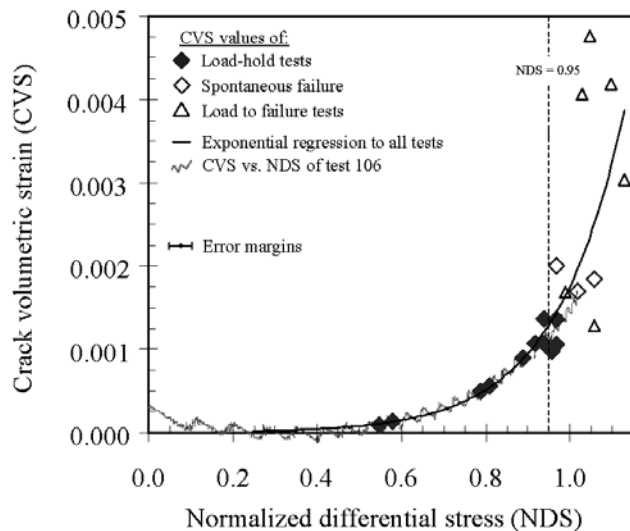


**Figure 3.** Crack volumetric strain, CVS (equation (4)), as a function of axial stress. Solid diamonds indicate CVS values calculated for the preselected maximal stress (start of the holding period); open symbols indicate CVS values calculated just before failure (for the failed tests). The thin curve is the exponential regression curve for all data points (equation (6)); the zigzag curve shows the continuous variations of CVS during test 106 (the zigzag shape reflect loading artifacts).

as indicating the poorly controlled volume increase associated with the failure stage.

#### 4. Microstructural Analysis

[18] The microstructural analysis focuses on the mode, dimensions, density and distribution of stress-induced microfractures in the deformed Mount Scott granite samples. The main objective is to understand the relationships between the microdamage described in this section and the rheological parameters described above and the theoretical damage models that are outlined later. To achieve this goal we mapped in detail the microfracture damage in four samples of MSG subjected to load-hold testing with maximum NDS values of 0.57, 0.88, 0.96 (unfailed) and 0.96 (failed), as well as one unstressed sample (samples 123, 114, 113, 110 and 157, respectively). The tests show negligible CVS increase during the hold time when  $NDS < 0.96$ , and thus the damage accumulated during the hold period is ignored.

##### 4.1. Mapping Methods

[19] The deformed samples were molded in epoxy resin after unloading and standard thin sections were made parallel to their long axes and at the central part of the cylinders (edges were excluded). In the faulted specimen (110), the thin section was also normal to the fault surface. The microstructural mapping was conducted by simultaneous manual digitization on the scanned computer image of the thin section ( $\times 150$  magnification) and visual examination of each fracture on a petrographic microscope ( $\times 40$ – $\times 200$  magnifications). We mapped only linear features that

display fracture characteristics: (1) some opening that indicate dilation and/or slip discontinuity (unlike grain boundaries that are sharp and tight); (2) continuity of the features along their trend (in contrast to the discontinuous appearance of fluid inclusion traces); (3) cross-cutting of grain boundaries. Segmented fractures were carefully examined for the nature of linkage between segments. Merged segments were mapped as one long fracture whereas separated segments were mapped as few separate fractures. The orientation change between segments did not affect this assessment. *Hadley* [1976] and *Moore and Lockner* [1995] treated a segmented fracture with intersegment orientation change of more than  $20^\circ$  as separate fractures. The shortest resolvable fractures were about 0.01 mm long whereas the longest mapped fractures were about three orders of magnitude longer. SEM images with magnification of  $\times 40$ – $\times 370$  (pixel size 0.002–0.0002 mm, respectively) were used for selected regions (Figure 4). The digitized microstructural data ([http://earth.es.huji.ac.il/reches/Publications/katz\\_2003\\_data.xls](http://earth.es.huji.ac.il/reches/Publications/katz_2003_data.xls)) are used to generate fracture maps, damage contour maps and microfracture orientations rose diagrams (Figure 5). We believe that the current approach of separate evaluation of each lineament is unbiased and complete.

[20] The microfracture density was calculated as the cumulative length of all mapped microfractures per unit area ( $\text{mm}/\text{mm}^2$  units). We calculated the mean microfracture density for the five maps in Figure 5, as well as the local density in 20–30 subregions for each of the maps; the subregions are  $25 \text{ mm}^2$  in size.

##### 4.2. Mode of Microfracturing

[21] The deformed specimens display two dominating microfracture groups: Group A with fractures trending subparallel to the loading axis ( $350^\circ$ – $010^\circ$  in Figure 5 where  $360^\circ$  is the direction of the loading axis), and group B with fractures trending in the intervals of  $320^\circ$ – $349^\circ$  and  $11^\circ$ – $40^\circ$  off the loading axis. These groups account to more than 80% of the mapped fractures (Table 3).

[22] Fractures of group A typically consist of one intragranular segment that is less than  $5 \mu\text{m}$  wide and less than 1 mm long (Figure 4a, and lower left of Figure 4d), with infrequent linkage to other fractures. Their geometry suggests initiation as intragranular fractures and growth to the boundaries of the host grain. We regard the fractures of this group as tensile microfractures subparallel to  $\sigma_1$ . The fractures of group B are up to  $10 \mu\text{m}$  wide with brecciated material in their core and they are typically composed of a few coalesced segments (Figures 4b and 4e). In places two segments overlap to form dilational or contractional jogs (Figure 4c, center of Figures 4d and 4f). Occasionally, the tips of fractures in this group are bent to become subparallel to the sample axis (Figures 4e–4f). The fractures of this group are frequently organized in relatively long, quasi-continuous bands of coalescing microfractures (e.g., Figure 4g). In several conspicuous cases these intergranular bands are 3–5 mm long (Figures 5c–5e) with spacing of few millimeters (Figure 5). We conclude that group B includes shear microfractures that most likely initiated at grain boundaries; however, we did not find evidence for displacement along these fractures. The microfractures that do not fall into the above two groups are probably reactivated preexist-

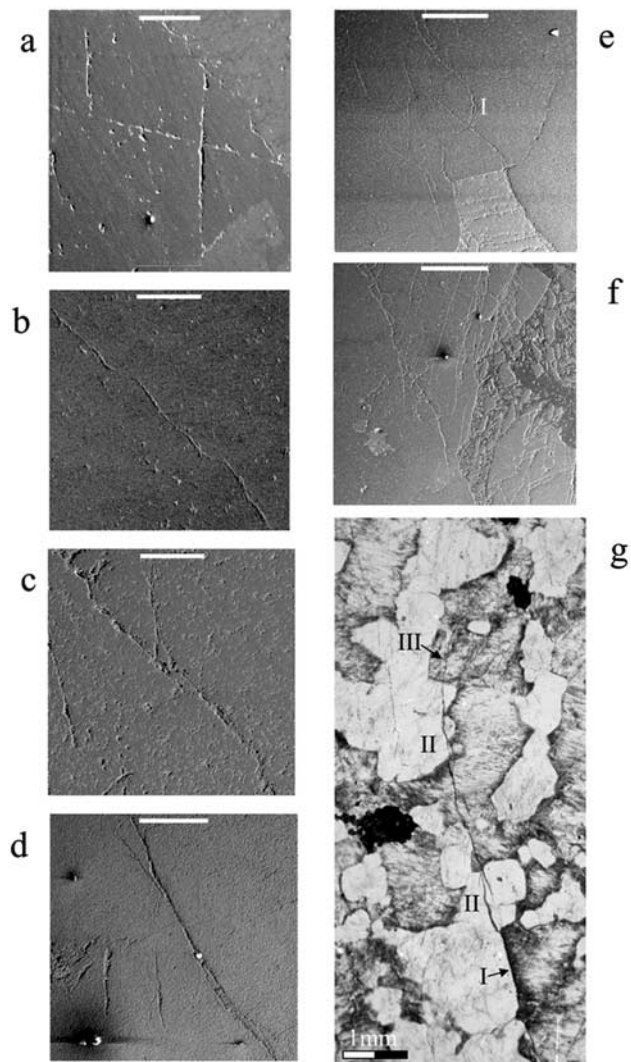


**Figure 4.** SEM images of microfractures in the MSG (locations in Figure 5). Maximum shortening is north-south; the scale bar is 100  $\mu\text{m}$  in Figures 4a–4c, 400  $\mu\text{m}$  in Figure 4d, and 600  $\mu\text{m}$  in Figures 4e–4f. (a) Intragranular, tensile (axis parallel) fracture in quartz (darker area); note the opening along the northeastern grain boundary, whereas the southern remained closed (specimen 114, NDS = 0.88). (b) Shear microfracture with linking segments (specimen 114, NDS = 0.88). (c) Shear microfracture with two overlapping segments and development of wing cracks (upper center) (specimen 110, NDS = 0.96 (spontaneous failure)). (d) Shear microfracture showing the initial stage of breccia development; note the two shorter tensile fractures in the lower left (specimen 110, NDS = 0.96 (spontaneous failure)). (e) Shear and tensile fractures in quartz grain (upper half) and open cleavage and grain boundary fractures in plagioclase (lower half). The tip of the shear fractures rotates to the stress direction (I) (specimen 110, NDS = 0.96 (spontaneous failure)). (f) The main fault cutting specimen 110 (right side of image), consisting of breccia with tensile and shear fractures to its left. (g) A band of shear microfractures (specimen 110, NDS = 0.96 (spontaneous failure)) that locally follows the grain boundary (I), displays segments coalesce (II), and activates

ing flaws that might coalesce with shear fractures to facilitate the formation of the long, segmented bands (Figure 4e).

### 4.3. Evolution of the Microfracture Patterns

[23] The maps in Figure 5 display the microfracture pattern from the undeformed sample (Figure 5a) to the failed one (Figure 5e). By assuming negligible variability between the original samples, we regard these maps as indicating the microfracture evolution during a single experiment. The undeformed sample displays low microfracture density with one preferred direction of fractures. The fracture pattern in specimen 123 (NDS = 0.57) displays one set of short, intergranular tensile microfractures (Table 3 and Figure 5b). Under higher stress, the relative frequency of the tensile microfractures decreases (group A in Figure 5c) and the relative frequency of shear microfractures (group B) increases (Figures 5c–5e and 6a). The microfracture density increases fairly systematically (Table 3 and Figures 5c–5e), yet there is no significant change in the relative length distribution of the microfractures (Figure 6b).

[24] The microfracture density varies in space. For example, the maximum local density of a single subregion (25  $\text{mm}^2$  in area) is about 2.0  $\text{mm}/\text{mm}^2$  just before failure (#113, NDS = 0.96), whereas the mean density of this sample is 1.11  $\text{mm}/\text{mm}^2$ . The failed sample (#110, NDS = 0.96) does not show higher density and its maximum local density of a single subregion is 1.8  $\text{mm}/\text{mm}^2$  ([http://earth.es.huji.ac.il/reches/Publications/katz\\_2003\\_data.xls](http://earth.es.huji.ac.il/reches/Publications/katz_2003_data.xls)). We thus conclude that the crosscutting fault did not induce significant additional microfractures to the host rock, and that 2.0  $\text{mm}/\text{mm}^2$  is the critical microfracture density before faulting. Finally, specimen 110 that was loaded to NDS = 0.96 and failed, includes a 2 mm wide fault with two large, linked segments (Figure 5e). The fault core is made of breccia that is highly crushed in its center and less crushed in its margins (Figure 4f).

## 5. Damage Analysis

### 5.1. Theoretical Derivations

[25] *Kachanov* [1992] presented several models that predict the reduction of the effective modulus of an elastic solid due to multiple distributed cracks. This reduction is assumed to be the sum of the contributions of all cracks where the crack density is quantified by  $\rho$ , a dimensionless parameter that in two dimensions is defined as

$$\rho = (1/A)\Sigma L^2, \quad (7)$$

where  $A$  is the representative area and  $L$  is half the crack length and  $\Sigma$  indicates summation of all cracks in the area  $A$ . Our damage measurements were done on two-dimensional (2-D) thin sections and these 2-D damage data cannot be converted into 3-D damage values (see Appendix A). Thus the present analysis is based on 2-D approximations as discussed in Appendix A.

[26] In this section we briefly outline three damage models and compare their predictions with our observations. The first is the model with 2-D array of “noninteracting cracks” that are randomly distributed in an isotropic matrix.

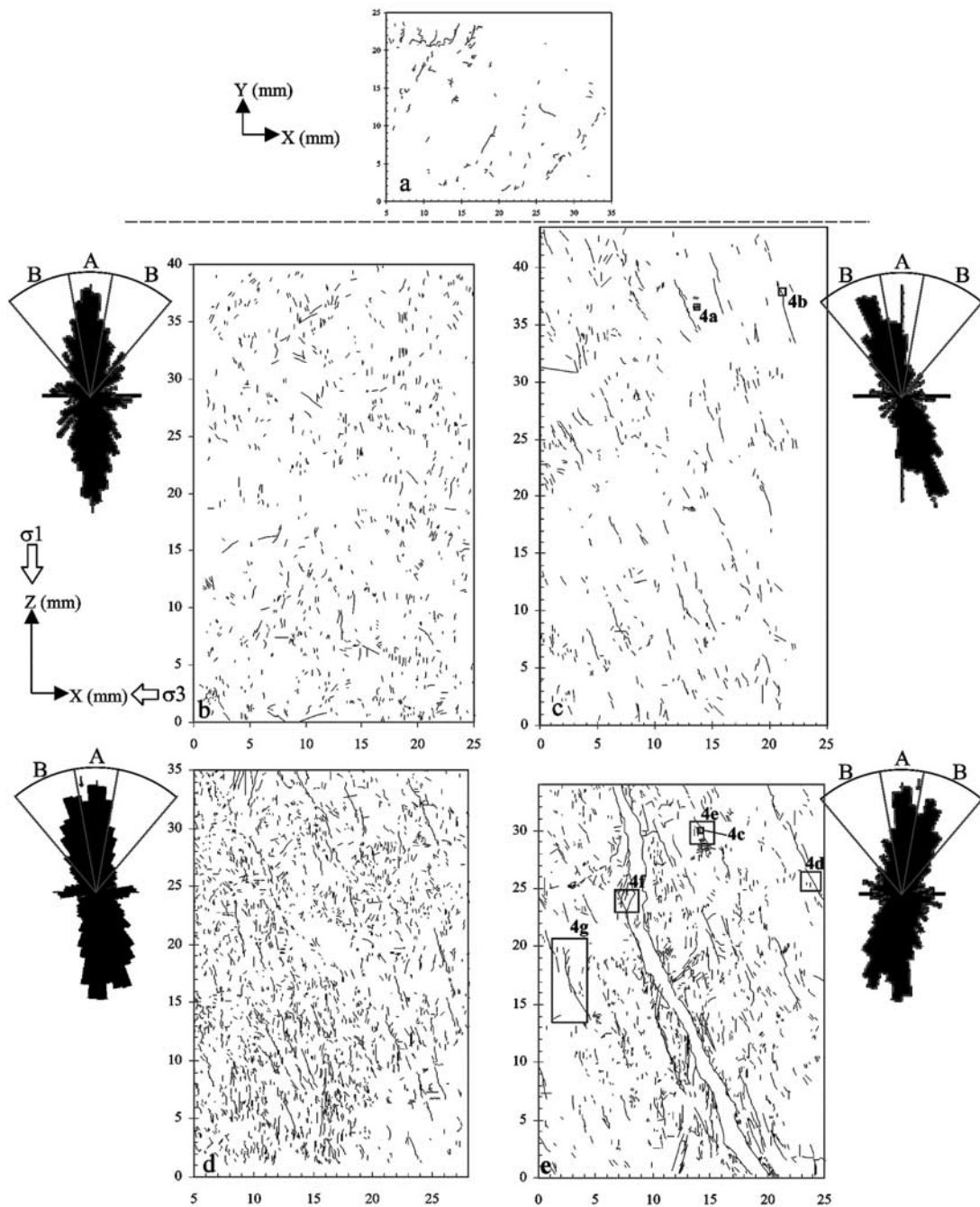


**Figure 5.** Microstructural maps showing microfractures in the five mapped thin sections. The thin sections of the deformed samples (Figures 5b–5e) are oriented parallel to Z, the long axis of the specimen, that is the direction of  $\sigma_1$ . The thin section of the undeformed sample (Figure 5a) is normal to the Z axis (note the marked axes). The rose diagrams are of the microfractures length-azimuth relations in area-weighted  $5^\circ$  sectors for Figure 5b–5e. The  $\sigma_1$  axis is the north axis of the associated fractures maps; the groups A and B on the rose diagrams include the sectors of  $320^\circ$ – $349^\circ$  and  $11^\circ$ – $40^\circ$  off the loading axis that correspond to the groups of tensile and shear microfractures, respectively (see text). (a) Specimen 157, unstressed. (b–d) Specimens 123, 114, and 113, maximum NDS of 0.57, 0.88, and 0.96, respectively. (e) Specimen 110, loaded to NDS = 0.96, followed by spontaneous failure.

*Kachanov* [1992] showed that the modulus reduction of this model behaves as

$$(E'/E_0) = 1/(1 + \pi\rho), \quad (8a)$$

where  $E'$  is the “effective deformation modulus” (see Appendix A) at a given stage and  $E_0$  is the effective deformation modulus at the linear stage of the stress-strain curve. *Kachanov* [1992] further reviewed other approxima-

**Table 3.** Results of Microstructural Damage Mapping<sup>a</sup>

Test	Maximum Stress (NDS) <sup>b</sup>	Map Area, <sup>c</sup> mm <sup>2</sup>	Number of Microfractures (All Groups) for Each Length Interval, mm						Microfracture Density <sup>d</sup>		Microfracture Type (Fraction of Total Length) <sup>e</sup>		
			0.03	0.1	0.3	1	3	10	#/mm <sup>2</sup>	mm/mm <sup>2</sup>	Group A (Tensile)	Group B (Shear)	Others
157	0.00	500	0	1	34	84	15	2	0.27	0.17			
123	0.57	1000	1	21	372	503	28	0	0.92	0.36	0.46	0.38	0.16
114	0.88	1075	0	1	138	345	63	3	0.51	0.29	0.26	0.61	0.13
113	0.96	875	0	57	1274	1152	102	2	2.96	1.11	0.40	0.45	0.15
110	0.96	875	0	35	507	681	115	8	1.54	0.76	0.38	0.46	0.15

<sup>a</sup>See text.<sup>b</sup>Stress at start of holding period.<sup>c</sup>Area of microstructural mapping on the thin section.<sup>d</sup>Number of fractures divided to the map area (#/mm<sup>2</sup>) or cumulative fracture length divided to the map area (mm/mm<sup>2</sup>).<sup>e</sup>Cumulative length of the microfracture in each group normalized by the cumulative length of all microfractures. The raw microstructural data set can be obtained at [http://earth.es.huji.ac.il/reches/Publications/katz\\_2003\\_data.xls](http://earth.es.huji.ac.il/reches/Publications/katz_2003_data.xls).

tions of the effective deformation modulus. The second model is the “self consistent scheme” of *Budiansky and O’Connell* [1976], that considers an isolated crack in a medium with an effective (reduced) modulus. This model predicts the following for 2-D randomly distributed cracks [after *Kachanov*, 1992]:

$$(E'/E_0) = (1 - \pi\rho). \quad (8b)$$

In this approximation the interactions always lead to reduction of the overall modulus. The reduction effect is not necessarily justified as the interactions could lead to shielding and hardening. Equation (8b) predicts that the modulus vanishes as the density approaches the cut off density of  $\rho = 1/\pi$  when the material disintegrates and fails. *Budiansky and O’Connell* [1976] suggested that the effective modulus at  $\rho = 1/\pi$  is very small but not zero. *Kachanov* [1992] used computer simulations of 2-D arrays to suggest that  $(E'/E_0) \sim 0.5$  for  $\rho = 0.3$ .

[27] A third model presented by *Kachanov* [1992] is the “differential scheme,” which also considers one isolated crack within an effective matrix, but the calculations are done incrementally with increasing by small  $d\rho$  steps and recalculation of the effective modulus of the matrix at each step. This scheme generates the following for 2-D randomly distributed cracks:

$$(E'/E_0) = e^{-\pi\rho}. \quad (8c)$$

There is no cut off density here and similarly to (8b) the interactions always lead to softening.

## 5.2. Comparison of Model Predictions and Experimental Observations

[28] We first note that  $E'$ , the “effective deformation modulus” of *Kachanov* [1992], is equivalent to the local slope of the stress-strain curve and thus it is identical to the deformation modulus  $D$  of the present analysis (equation (3a)). This implies that

$$(D/D_{\max}) = (E'/E_0), \quad (9)$$

where  $D_{\max}$  is defined in equation (3b). We now use equations (8a)–(8c) to calculate the theoretically expected ratio  $(E'/E_0)$  for the damage  $\rho$  measured in the five

samples and then compare the calculated ratios with the experimentally measured ratios of  $(D/D_{\max})$  for the same samples. For this comparison, the damage intensity  $\rho$  is calculated by applying the summation equation (7) to all microfractures according to their individual length in our microstructural mapping (Figure 5). While other measures of the fracture length can be used (e.g., cumulative length in binned length intervals by *Hadley* [1976] and *Reches and Lockner* [1994]), we did not use binned data as there is no standard procedure to select the bins and their width. The method used here does not depend on the binning procedure.

[29] Figure 7a displays the calculated modulus ratios  $(E'/E_0)$  for the five samples (Table 3) according to the three models (equation (8)) versus the experimentally measured ratios of  $(D/D_{\max})$ . It should be noted that no adjusting factor was used to scale the modulus ratios, and the marked solid line indicates perfect agreement between measured and calculated ratios. We first note that the “noninteracting cracks” model (equation (8a)) predicts the smallest intensity of modulus reduction (solid squares), whereas the “self-consistent scheme” (equation (8b)) predicts the largest modulus reduction (solid diamonds). Second, for  $\rho < 0.06$  the modulus ratio  $(E'/E_0)$  predicted by the three models is smaller than the measured  $(D/D_{\max})$ . We think that this deviation indicates the high sensitivity to mapping errors in samples with low damage intensity, and the fact that slight damage can be observed even in undeformed samples. Third, for  $\rho > 0.06$ , the  $(E'/E_0)$  ratio of the “noninteracting cracks” model (solid squares) is in very good agreement with the measured  $(D/D_{\max})$  ratio. The other two models overestimate the modulus reduction. In summary, from the three examined models, the “noninteracting cracks” model fits best the observations.

[30] Further the “noninteracting scheme” of *Kachanov* [1992] appears to be valid even for high crack densities ( $\rho \sim 0.2$ ) that are expected to induce interactions (specimens 110, 113). Similar results are found with computer experiments of *Kachanov* [1992] and *Davis and Knopoff* [1995], that ran high density ( $\rho > 0.2$ ) synthetic 2-D crack arrays. They suggested that shielding and amplification interaction effects are canceling each other [*Kachanov*, 1992] and that each crack is subjected to a stress field that is approximately the field at infinity even with high densities of cracks [*Davis and Knopoff*, 1995].

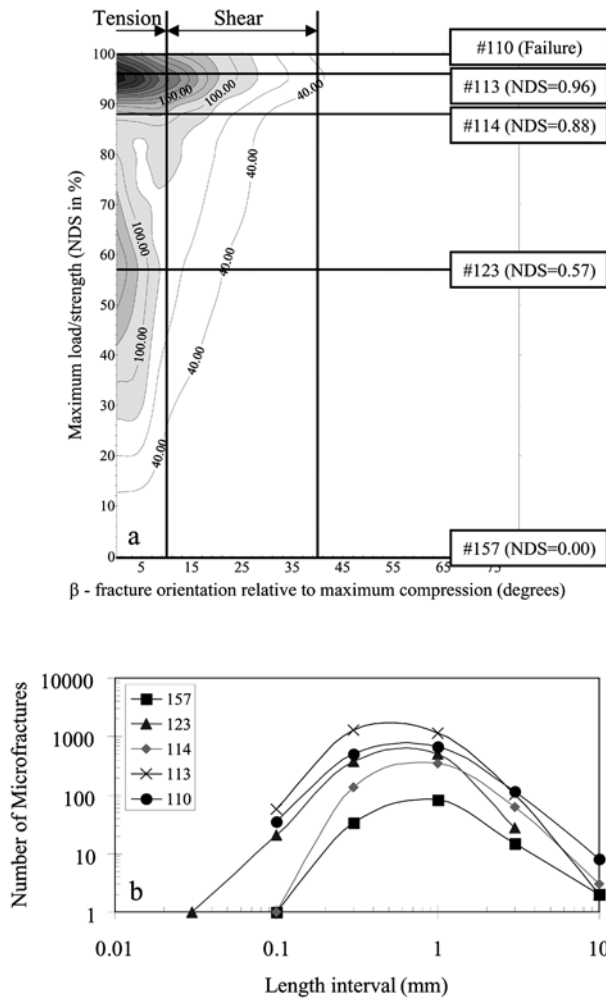


**Figure 6.** Variations of microfracture characteristics with loading. (a) The frequency of microfractures length distribution with respect to  $\sigma_1$  axis for the five mapped samples. The contours indicate the variations of an arbitrary parameter (the microfracture length (mm) measured at given angle  $\beta$  for the marked NDS). The calculations are for  $10^\circ$  intervals; for example, in sample 123 (NDS = 0.57) we mapped 42 mm of fractures with  $\beta = 25^\circ \pm 5^\circ$ , whereas in sample 113 (NDS = 0.96) we found 120 mm of fractures in the same angle interval. Note division into tensile ( $\beta = 0^\circ - 10^\circ$ ) and shear ( $\beta = 11^\circ - 40^\circ$ ) fractures and the absolute and relative increase of shear fractures with stress increase (see text). (b) Frequency (number of microfractures) fit into each length interval for specimens 157 (NDS = 0.00), 123 (NDS = 0.57), 114 (NDS = 0.88), 113 (NDS = 0.96), and 110 (NDS = 0.96, and failure).

[31] We can use the “noninteracting cracks” model to calculate damage intensity for the experiments by rearranging equation (8a) and using equation (9):

$$\rho = (D_{\max}/D - 1)/\pi. \quad (10)$$

Figure 7b displays the damage intensity calculated for all tests by using equation (10) and the experimental ( $D/D_{\max}$ ) at the corresponding maximum NDS (diamonds). Also plotted

are the exponential best-fit curve of these data points (thick curve), the continuous  $\rho$  for test 106 (thin curve), and the mapped  $\rho$  in the five samples of Figure 7a (open squares). This plot indicates a strong nonlinear increase in  $\rho$  toward failure with  $\rho \approx 0.20$  at NDS  $\approx 0.95$  that corresponds to  $(E'/E_0) \sim 0.61$  (equation (8a)). This value is in agreement with the experimental values of  $(D/D_{\max}) = 0.65 \pm 0.02$  for specimens loaded close to failure (113 and 110 in Table 4).

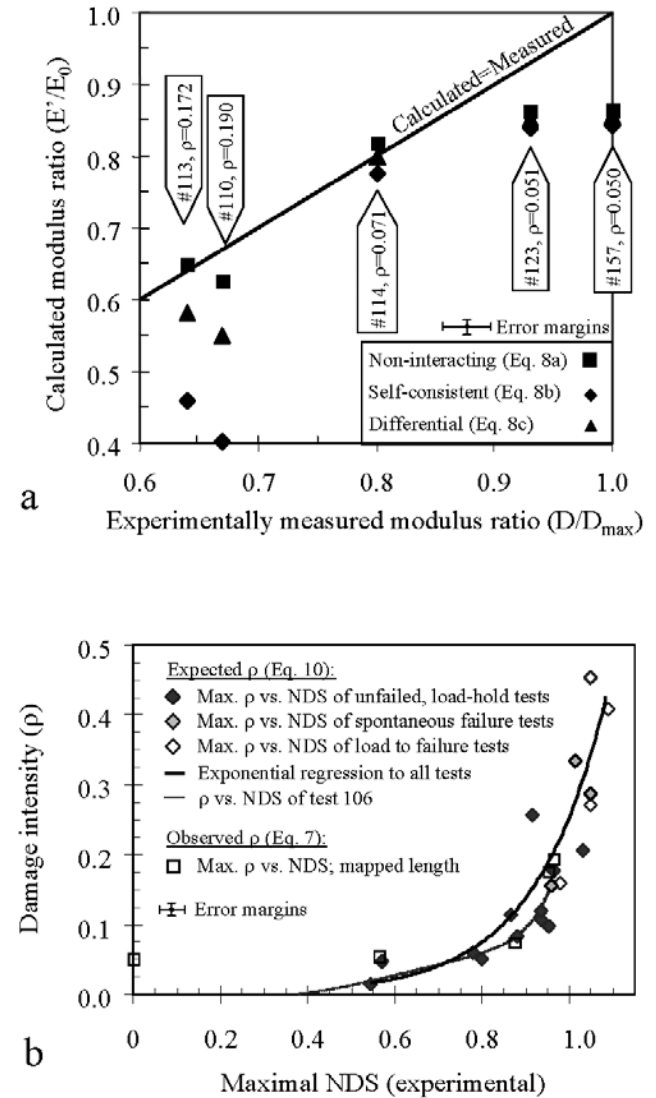


**Figure 7.** (a) The relationships between expected modulus ratio ( $E'/E_0$ ) calculated from the damage intensity ( $\rho$  in equation (7)) and the experimentally measured values of  $(D/D_{\max})$  for the same samples (see text). The same data are plotted for the three models of equation (8) as marked in the legend; the solid line indicates exact agreement between expected and measured values. (b) Expected damage intensity  $\rho$  in the present tests, calculated for maximum stress of all tested samples using equation (10) (diamonds), including the best-fit exponential curve (thick curve,  $\rho = 0.0006 \exp(6.11 \text{ NDS})$ ,  $R^2 = 0.78$ ). Also plotted is the calculated continuous  $\rho$  for one test (106) (thin curve) and the observed damage intensity in the five samples (open squares, same data as solid squares in Figure 7a).

**Table 4.** Microstructural Damage Intensity Parameters

Test	Maximum Stress (NDS)	Deformation Modulus Ratio (Experimental) $(D/D_{\max})^a$	Damage Density $\rho^b$				$S/L^c$
			Group A (Tensile)	Group B (Shear)	Others	Total	
157	0.00	1.00				0.050	3.1
123	0.57	0.93	0.019	0.019	0.012	0.051	2.7
114	0.88	0.80	0.014	0.048	0.009	0.071	2.4
113	0.96	0.64	0.063	0.093	0.016	0.172	1.6
110	0.96	0.67	0.060	0.098	0.032	0.190	1.6

<sup>a</sup>Ratio of the modulus at hold point and the maximum modulus (Table 2).

<sup>b</sup>Calculated using equation (7) by summation of all microfractures (separated to groups) according to their measured, individual lengths.

<sup>c</sup>Calculated spacing/length ratio using equation (11) for the entire fracture population [after *Reches and Lockner, 1994*].

[32] *Lockner et al. [1992]* used the  $S/L$  parameter to describe microfracture density, where  $S$  is fracture spacing and  $L$  is the fracture length. *Reches and Lockner [1994]* proposed that brittle rocks fail when the microfractures interact in a self-organized fashion that leads to macroscopic faulting. They showed that when  $S/L \geq 1$  the induced stresses between neighboring fractures is smaller than 1% of the fracturing stresses and thus the interactions can be ignored. *Reches and Lockner* used the data of *Hadley [1976]* to show that in undeformed specimens  $S/L = 1-4$ , and in failed specimens  $S/L \approx 0.35$ , and estimated that  $S/L \approx 0.5$  is the critical value for yielding. *Reches and Lockner [1994]* showed that for random fracture distribution,

$$S/L \sim \sqrt{1/(\gamma L^2)}, \quad (11)$$

where  $\gamma$  is the microfracture density in terms of number of cracks per unit area. We calculated  $S/L$  for the five mapped samples by substituting the measured crack length data (Table 3) into equation (11), and found that  $S/L$  decreases nonlinearly with stress and it is  $\sim 1.6$  at failure (Table 4). This relatively high value of  $S/L$  at failure (relatively low microfracture density) suggests that the failure mechanism of MSG differs from the failure mechanism derived by *Reches and Lockner [1994]* (see section 6).

### 5.3. Critical, Local High Damage Intensity

[33] The underlying assumption in the above analysis is that the samples deformed uniformly with quasi-uniform damage distribution, and that a single value deformation modulus is sufficient to describe the entire sample. This assumption is examined here. We showed above that deformation modulus can be estimated from microfracture density. Thus the fracture maps (Figure 5) can be converted into maps of model prediction of  $(E'/E_0)$ . This is done by calculating the local  $\rho$  in 20–30 subregions (each 25 mm<sup>2</sup> in size) of the maps (equation (7)), and then using equation (8a) to obtain the  $(E'/E_0)$  of the subregions. Figure 8 presents the contoured maps of this ratio.

[34] Figure 8 indicates that the variability of modulus distribution  $(E'/E_0)$  increases with loading. In specimens 113 and 110, the value of  $E'/E_0 < 0.6$  dominate most of the mapped area but several patches of localized damage show lower  $E'/E_0$  values that could indicate local rock failure that could lead to the failure of the entire specimen.

[35] The modulus maps of Figure 8 show that the samples are composed of zones that are relatively strong and patches

of degraded, weak rock. When the patches of localized damage grow and the continuity of the strong matrix is eliminated, the rock would fail. For example, it is possible that sample 113 did not fail because a zone of low density with  $0.7 < E'/E_0 < 0.8$  crosses the specimen from side to side (Figure 8d). A different situation appears in specimen 110 where a zone of low  $E'/E_0 < 0.6$  cuts the specimen almost top to bottom and probably enables failure (Figure 8e).

## 6. Discussion: Failure Mechanism of Mount Scott Granite

### 6.1. Failure of Brittle Rocks

[36] It is generally accepted that growth and interaction of microcracks control macroscopic faulting. One group of faulting models proposes that a fault grows in the wake of a process zone that is a finite size region of high stress concentration at fault tip in which the intact rock is disintegrated [*Cowie and Scholz, 1992; Reches and Lockner, 1994*]. This concept predicts that fault related damage, mostly tensile microfractures, would be restricted to the fault vicinity and will decay away from the fault. Another group of models assumes that a fault forms due to interaction among many damage points, mostly microcracks, which formed prior to faulting. These microcracks are assumed to coalesce when their density reaches a critical value [*Peng and Johnson, 1972; Horii and Nemat-Nasser, 1985; Ashby and Sammis, 1990; Lyakhovskiy et al., 1997a*]. This concept implies that microcracks are not necessarily restricted to the fault tip, and that the density of microcracks away from the fault would be comparable to the microcrack density along the initial fault.

[37] It is also commonly accepted that tensile microfractures dominate the prefailure damage of brittle, crystalline rocks, following, for example, the observations of *Hadley [1976], Tapponnier and Brace [1976], Reches and Lockner [1994], and Moore and Lockner [1995]*. As the tensile microfractures form even under high confining pressures, their formation is attributed to induced tension at the tip of shear fractures that generates the well-known “wing crack” systems [*Tapponnier and Brace, 1976; Germanovich et al., 1994; Reches and Lockner, 1994*]. While the “parent” shear fractures are only seldom observed [e.g., *Tapponnier and Brace, 1976; Schulson et al., 1999*], the wing crack configuration is often used as the main mechanism of tensile fracturing under compression [*Horii and Nemat-Nasser, 1985; Ashby and Sammis, 1990; Germanovich et al., 1994*].

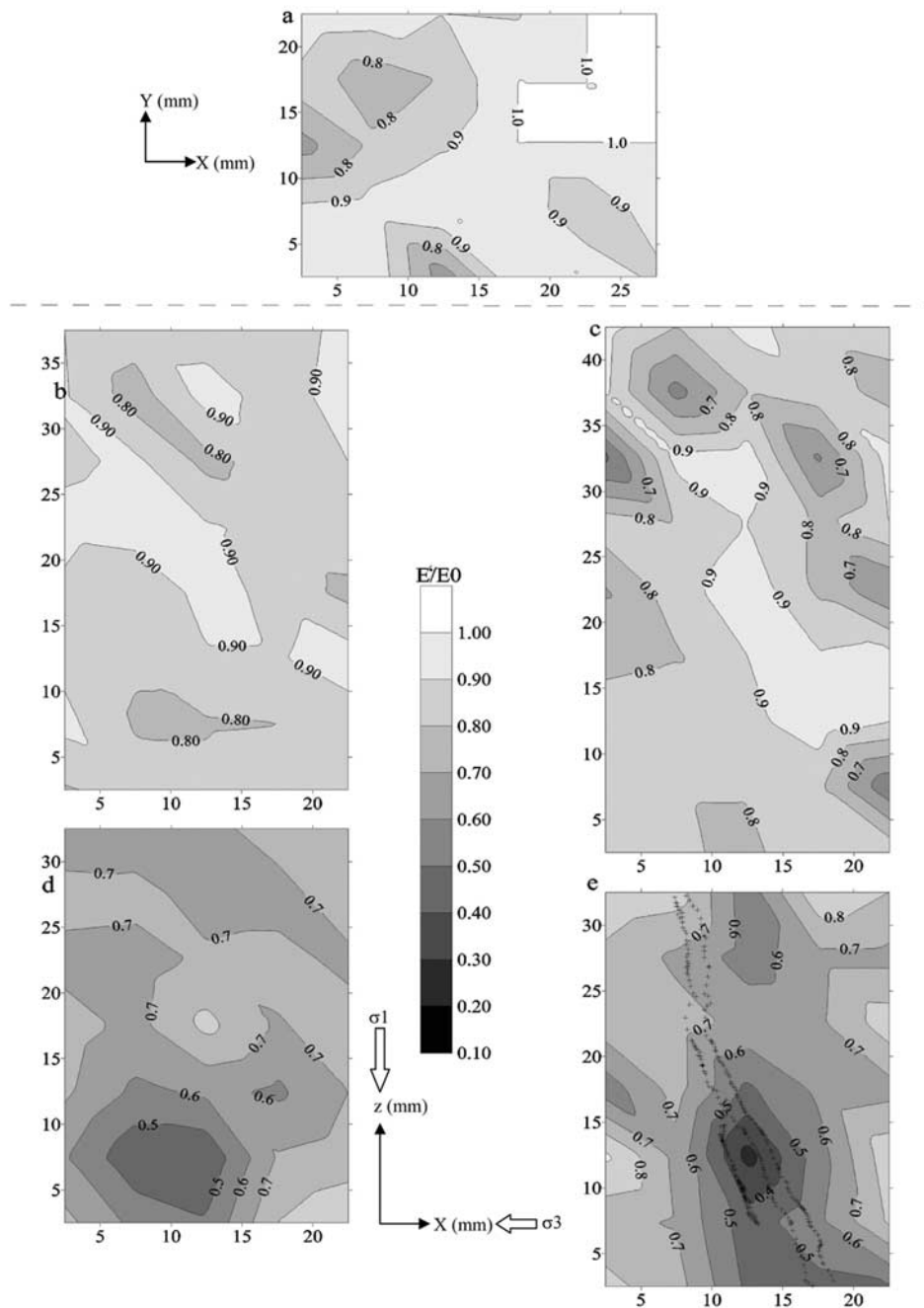


**Figure 8.** Expected local values of the deformation modulus ( $E'/E_0$ ) calculated with equation (8a) for the mapped samples (see text). The contours indicate the ( $E'/E_0$ ) values with hatch on the ( $E'/E_0$ ) = 0.6 contour. (a–e) Specimens 157, 123, 114, 113, and 110. Crosses in specimen 110 are the fault trace (not included in the modulus calculation).

[38] The systematic study of microfractures in the present study allows us to explore mechanism of failure in Mount Scott granite, as we do in the sections below.

## 6.2. Failure by Growth and Coalescence of Shear Microfractures

[39] We first compare the failure features of Mount Scott granite with those of the well-studied Westerly granite [e.g., Hadley, 1976; Lockner *et al.*, 1992]. The mean grain size of Westerly granite is smaller, about 0.2 mm versus

0.9 mm in MSG. The measured microfracture density is higher in Westerly granite, and it is about  $18 \text{ mm/mm}^2$  at failure [Hadley, 1976], that is, significantly higher than the  $2.0 \text{ mm/mm}^2$  density of MSG. In the pre-faulting stage, the majority of the Westerly granite microfractures are axial tensile cracks, and during failure, microfractures with deviation by  $20^\circ$ – $60^\circ$  from the specimen axis developed close to the tip of the propagating fault [Moore and Lockner, 1995]. As a consequence, microfracture density is twice as high in the fault vicinity than away from the

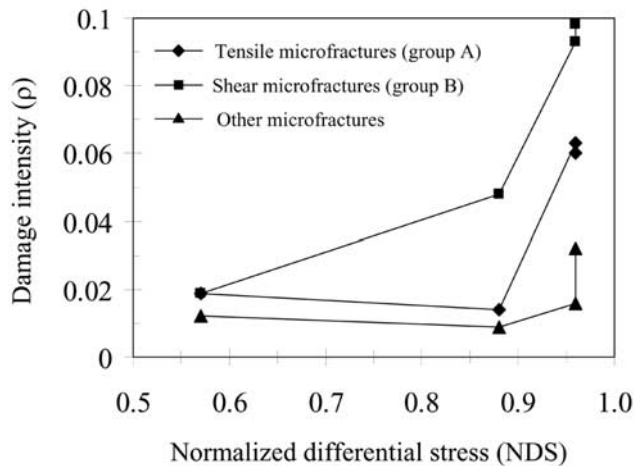


**Figure 9.** The damage intensity  $\rho$  for the present tests calculated separately for the tensile microcracks (group A), shear microfractures (group B), and the other microfractures. Data are shown in Table 4.

fault. On the basis of these observations, the model of *Reches and Lockner* [1994] suggests that Westerly granite fails by interaction of tensile microfractures and fault induced tensile fracturing.

[40] Apparently, this model cannot explain the failure of Mount Scott granite. First, MSG has lower microfracture density that hardly enables interaction ( $S/L \sim 1.6$ , see above). Second, the high density of microfractures in specimens loaded to failure is not spatially associated with the fault (Figure 5e). Third, the relative frequency of the microshears increases with stress (Table 3) as well as the damage,  $\rho$ , associated with them (Table 4, Figure 9). Four, many of the microshears are arranged in elongated, quasi-continuous intergranular bands (Figures 4g and 5c–5e), whereas the tensile microcracks are typically intragranular (Figure 5). Hence while the initial damage of MSG (for  $NDS < 0.6$ ) is equally associated with tensile and shear microfractures (Table 4, Figure 9), the later damage is dominated by the intergranular bands of microshears (Figures 4g, 5, and 9).

[41] Following these observations, we envision that the failure of MSG is controlled by microshears. The axial load increase leads to increase in relative density of the microshears and their arrangement in elongated bands of coalescing microfractures (Figures 4g and 5c–5e). Eventually, the macrofault forms by facilitating the existing, coalesced microshears; the additional damage generated during the macrofault propagation is apparently small.

[42] Microshear development is not unique to Mount Scott granite. *Janach and Guex* [1980] suggested that under sufficiently high confining pressure the local tensile stresses are suppressed and the micro deformation should be dominated by microshears. *Escartin et al.* [1997] found microshears with negligible tensile fracturing close to the fault plane in serpentinite rocks loaded to failure under confining pressure of 50 MPa. The failure was accompanied with minor crack volumetric strain, as microshears generate less volume change than tensile fractures [*Escartin et al.*, 1997]. The microshears in the serpentinite use cleavage planes of serpentine that deviate about  $30^\circ$ – $60^\circ$  from  $\sigma_1$ ; hence, the

fracture energy of shear along the serpentine cleavage is lower than the other possible fracturing in that rock [*Escartin et al.*, 1997]. Similar behavior was found for Gevanim quartz-syenite (southern Israel). This rock lack tensile microcracks in both naturally faulted samples [*Katz et al.*, 2003] and triaxially failed samples [*Katz and Reches*, 2000].

[43] The development of micros shears, with or without tensile microcracks, is not anticipated as the fracture toughness of mode I fractures,  $K_{IC}$ , is usually smaller than the fracture toughness of mode II fractures,  $K_{IIc}$ . Yet the observations mentioned above and in additional analyses (B. Haimson and C. Chang, personal communication, 2001) indicate that micros shears are too common to be ignored. A detailed discussion of this topic is the subject of our ongoing work (O. Katz et al., manuscript in preparation, 2003).

## 7. Conclusions

[44] The present analysis is focused on damage evolution, nonlinear rheology, and brittle failure mechanisms in Mount Scott granite; the main results are outlined below.

### 7.1. Damage and Strength

[45] 1. The prefailure damage includes shear and tensile microfractures and their density increases with increasing stresses. The shear microfractures form intergranular bands of coalescing fractures whereas the tensile microfractures are primarily intragranular;

[46] 2. With increasing stress, the rock mechanical quality undergoes monotonous, nonlinear degradation and the deformation modulus drops to as low as 0.65 its maximum value;

[47] 3. Spontaneous failure occurs above a threshold stress of about 0.95 the ultimate strength above which the damage increases nonlinearly even under constant stroke.

### 7.2. Nonlinear Damage Rheology

[48] The observed microstructure damage and the experimental, macroscopic rheology are integrated for the comparison between measured and predicted damage. From the three examined models, the observed microfracture density fits best the predictions of the “noninteracting cracks” model in isotropic matrix, derived by *Kachanov* [1992] even for high microfracture density ( $\rho \sim 0.2$ ). To the best of our knowledge, this is the first experimental corroboration of a stress-induced damage model.

### 7.3. Failure Mechanisms

[49] The damage in Mount Scott granite is quasi-uniformly distributed and dominated by intragranular tensile microfractures and intergranular microshears. With increasing stress, the density and damage of microshears increase and they coalesce to form elongated bands; eventually the macrofault forms by coalescing the existing microshears bands. Apparently, the interactions among tensile microfractures do not contribute significantly to the failure of MSG as was recently observed for other rocks.

## Appendix A

[50] A central issue in the present study is the choice of a suitable reference system for the damage analysis. In triaxial tests the samples are loaded by axisymmetric, 3-D stress state with  $\sigma_1 > \sigma_2 = \sigma_3$ , and on the other hand, the damage is

mapped on 2-D thin sections. There is no practical method to determine the 3-D geometry of the microfractures in the thin sections as they appear as linear features that cannot be traced into the third dimension. Two approaches were used to overcome this limitation. Hadley [1976] assumed that the microfractures are penny-shaped in three-dimensions and calculated the 3-D damage by using 2-D measurements. This assumption however, has no observational or theoretical support for triaxial, axisymmetric loading.

[51] We use here a different approach and analyze the measured damage and the theoretical predictions in terms of 2-D approximations. The loading conditions applied on a thin section that parallels the long axis of a triaxial sample is  $\sigma_1 > \sigma_2 = \sigma_3$ , where  $\sigma_1$  and  $\sigma_2$  ( $=\sigma_3$ ) are within the thin section plane and  $\sigma_3$  ( $=\sigma_2$ ) is normal to it (Figure 5). This configuration is bounded by the plane-stress state of  $\sigma_1 > \sigma_2$  and  $\sigma_3 = 0$  that is normal to the thin section, and by the plane-strain state of  $\sigma_1 > \nu(\sigma_1 + \sigma_3) > \sigma_3$ , where  $\nu$  is the Poisson ratio and  $\sigma_1$  and  $\sigma_3$  are within the section plane. Using the 2-D approximation allows us to compare directly between the measured 2-D damage and the predictions of 2-D models (equation (8) [after *Kachanov*, 1992]). Substituting our experimental results into *Kachanov's* [1992] equations (1.6) and (2.13) shows that the reduction of the Young modulus predicted by the plane-stress deviates by less than 5% from the plane-strain prediction. As this deviation is small, we used *Kachanov's* solution for plane-stress (equations (8) and (9)), and mark the Young modulus as  $E'$  to indicate this approximation.

[52] Finally, we believe that future improvements of X ray CT techniques [*Karacan et al.*, 2001] will allow the determination of the actual 3-D geometry of microfractures. Once this happens, assumptions and approximations like those by *Hadley* [1976] or the present study could be eliminated.

[53] **Acknowledgments.** Charles M. Gilbert kindly provided the samples of Mount Scott granite for this study as well as useful comments. The laboratory work was conducted at the Rock Mechanics Institute, University of Oklahoma, Norman, with the invaluable help and advice of J.-C. Roegiers, Gene Scott, and Pete Keller. Discussions with Vladimir Lyakhovsky significantly contributed to the quality of this study. Thanks to Rod Holcombe for the permit to use the GeOrient program. Many thanks to the careful reviews and insightful comments by two anonymous reviewers and the Associate Editor (Karen Mair) that significantly improved the manuscript. The study was supported, in part, by Eberly Family Chair funds of M. Charles Gilbert, the Rock Mechanics Institute, University of Oklahoma, Norman, the US-Israel BiNational Fund, grant 98-135, and the Geological Survey of Israel project 30225.

## References

- Ashby, M. F., and C. G. Sammis (1990), The damage mechanics of brittle solids in compression, *Pure Appl. Geophys.*, *133*, 489–521.
- Budiansky, B., and R. J. O'Connell (1976), Elastic moduli of a cracked solid, *Int. J. Solids Struct.*, *12*, 81–97.
- Cowie, P. A., and C. H. Scholz (1992), Physical explanation for the displacement-length relationship of faults using a post-yield fracture mechanics model, *J. Struct. Geol.*, *14*, 1133–1148.
- Cox, S. J. D., and P. G. Meredith (1993), Microcrack formation and material softening in rocks measured by monitoring acoustic emission, *Int. J. Rock Mech. Min. Sci.*, *30*, 11–24.
- Crampin, S. (1994), The fracture criticality of crustal rocks, *Geophys. J. Int.*, *118*, 428–438.
- Crampin, S., and C. M. Sayers (1994), Comment on "Crack models for a transversely isotropic medium" by C. H. Cheng and C. M. Sayers, *J. Geophys. Res.*, *99*, 11,749–11,753.
- Davis, P. M., and L. Knopoff (1995), The elastic modulus of media containing strongly interacting antiplane cracks, *J. Geophys. Res.*, *100*, 18,235–18,258.

- Escartin, J., G. Hirth, and B. Evans (1997), Nondilatant brittle deformation of serpentinites: Implications for Mohr-Coulomb theory and the strength of faults, *J. Geophys. Res.*, *102*, 2897–2913.
- Germanovich, L. N., B. J. Carter, A. V. Dyskin, A. R. Ingraffea, and K. K. Lee (1994), Mechanics of brittle fracture of rock with pre-existing cracks in compression, *Pure Appl. Geophys.*, *143*, 117–149.
- Hadley, K. (1976), Comparison of calculated and observed crack densities and seismic velocities in Westerly granite, *J. Geophys. Res.*, *81*, 3484–3494.
- Horii, H., and S. Nemat-Nasser (1985), Compression-induced microcrack growth in brittle solids: Axial splitting and shear failure, *J. Geophys. Res.*, *90*, 3105–3125.
- Janach, W., and L. H. Guex (1980), In-plane propagation of shear microcracks in brittle rocks under triaxial compression, *J. Geophys. Res.*, *85*, 2543–2553.
- Kachanov, M. (1992), Effective elastic properties of cracked solids: Critical review of some basic concepts, *Appl. Mech. Rev.*, *45*(8), 304–335.
- Karacan, C. O., A. S. Grader, and P. M. Halleck (2001), Mapping of permeability damage around perforation tunnels, *J. Energy Resour. Technol.*, *123*, 205–213.
- Katz, O., and Z. Reches (2000), Micro- and macro- structural analysis of small faults in a quartz-syenite intrusion: Faulting of a brittle rock without microcracking?, *Eos Trans. AGU*, *81*(48), Fall Meet. Suppl., Abstract T61F-05.
- Katz, O., M. C. Gilbert, Z. Reches, and J. C. Roegiers (2001), Mechanical properties of Mount Scott granite, Wichita Mountains, Oklahoma, *Okla. Geol. Notes*, *61*(2), 28–34.
- Katz, O., Z. Reches, and G. Baer (2003), Faults and their associated host rock deformation: Part I. Structure of small faults in a quartz-syenite body, southern Israel, *J. Struct. Geol.*, *25*, 1675–1689.
- Kranz, L. K. (1979), Crack growth and development during creep in Westerly granite, *Int. J. Rock Mech. Min. Sci.*, *16*, 23–36.
- Lockner, D. A., D. A. Moore, and Z. Reches (1992), Microcracks interaction leading to shear fracture, in *Rock Mechanics*, edited by J. R. Tillerson and W. R. Wawersik, pp. 807–816, A. A. Balkema, Brookfield, Vt.
- Lyakhovsky, V., Y. Ben-Zion, and A. Agnon (1997a), Distributed damage, faulting, and friction, *J. Geophys. Res.*, *102*, 27,635–27,649.
- Lyakhovsky, V., Z. Reches, R. Weinberger, and T. E. Scott (1997b), Non-linear elastic behavior of damaged rocks, *Geophys. J. Int.*, *130*, 157–166.
- Martin, C. D., and N. A. Chandler (1994), The progressive fracture of Lac du Bonnet granite, *Int. J. Rock Mech. Min. Sci. Geomech. Abstr.*, *31*, 643–659.
- Moore, D. E., and D. A. Lockner (1995), The role of microcracking in shear-fracture propagation in granite, *J. Struct. Geol.*, *17*, 95–114.
- Nur, A., and G. Simmons (1969), Stress-induced velocity anisotropy in rock: An experimental study, *J. Geophys. Res.*, *74*, 6667–6674.
- Peng, S. A., and M. Johnson (1972), Crack growth and faulting in cylindrical specimens of Chelmsford granite, *Int. J. Rock Mech. Min. Sci.*, *9*, 37–86.
- Price, J. D., J. P. Hogan, and M. C. Gilbert (1996), Rapakivi texture in the Mount Scott granite, Wichita mountains, Oklahoma, *Eur. J. Mineral.*, *8*, 435–451.
- Price, J. D., J. P. Hogan, M. C. Gilbert, and J. D. Payne (1998), Surface and near-surface investigation of the alteration of the Mount Scott Granite and geometry of the Sandy Creek Gabbro pluton, Hale Spring area, Wichita Mountains, Oklahoma, in *Basement Tectonics 12*, edited by J. P. Hogan and M. C. Gilbert, pp. 79–122, Kluwer Acad., Norwell, Mass.
- Reches, Z., and D. A. Lockner (1994), Nucleation and growth of faults in brittle rocks, *J. Geophys. Res.*, *99*, 18,159–18,174.
- Sayers, C. M., and M. Kachanov (1995), Microcrack-induced elastic wave anisotropy of brittle rocks, *J. Geophys. Res.*, *100*, 4149–4156.
- Schulson, E. M., D. Iliescu, and C. E. Renshaw (1999), On the initiation of shear faults during brittle compressive failure: A new mechanism, *J. Geophys. Res.*, *104*, 695–705.
- Scott, T. E., Q. Ma, J. C. Roegiers, and Z. Reches (1994), Acoustic tomographic difference imaging of dynamic stress fields, in *Rock Mechanics in Petroleum Engineering: Proceedings*, pp. 99–104, A. A. Balkema, Brookfield, Vt.
- Taponnier, P., and W. F. Brace (1976), Development of stress-induced microcracks in Westerly granite, *Int. J. Rock Mech. Min. Sci. Geomech. Abstr.*, *13*, 103–112.
- Turcotte, D. L., W. I. Newman, and R. Shcherbakov (2003), Micro- and macro-scopic models of rock fracture, *Geophys. J. Int.*, *152*, 718–728.
- Wawersik, W. R., and W. F. Brace (1971), Post-failure behavior of a granite and diabase, *Rock Mech.*, *3*(2), suppl., 61–85.

O. Katz, Geological Survey of Israel, 30 Malkhe Israel Street, Jerusalem 95501, Israel. (odedk@mail.gsi.gov.il)

Z. Reches, Institute of Earth Sciences, Hebrew University, Jerusalem 91904, Israel. (reches@earth.es.huji.ac.il)